

# Joint FWI of diving and reflected waves using a graph space optimal transport distance: synthetic tests on limited-offset surface seismic data

Giuseppe Provenzano\*, ISTERre, Univ. Grenoble Alpes; Romain Brossier, ISTERre, Univ. Grenoble Alpes; Ludovic Métivier, LJK, CNRS, Univ. Grenoble Alpes; Yubing Li, previously at ISTERre, Univ. Grenoble Alpes

## SUMMARY

Full waveform inversion (FWI) of limited-offset seismic reflection data achieves broadband imaging only in the shallow subsurface sampled by the diving waves. In order to image deeper targets, Reflection WI (RWI) exploits wavepaths generated by reconstructed reflectors to constrain the smooth part of the velocity field. Joint FWI (JFWI) complements the RWI kernel at shallow depths by inverting simultaneously for diving and reflected waves. The JFWI solution, used as starting model, provides FWI with the low wavenumbers necessary to converge to a broadband velocity. This approach is not immune to the inherent non-linearity of  $L^2$ -norm waveform inversion with respect to the wavefield kinematics, and benefits from the use of misfit functions robust to cycle-skipping. Here we attempt to reconstruct a complex subsurface from limited-offset streamer synthetic reflection data, using a 1D starting model. The strategy successfully combines JFWI with a graph-space Optimal Transport (GSOT) objective function, whereas  $L^2$ -based JFWI suffers from severe cycle-skipping. Furthermore, the results attest the benefits of jointly inverting for diving and reflected waves in JFWI.

## INTRODUCTION

Full waveform inversion (FWI, Lailly, 1983; Tarantola, 1984) is an iterative data fitting technique aiming at a high-resolution, broadband reconstruction of the subsurface elastic properties. Over the last few decades, this methodology has reached its maturity as a tool to obtain accurate acoustic velocity models of the subsurface (e.g. Virieux and Operto, 2009), as well as for the characterization of the elastic properties of complex exploration targets (e.g. Operto et al., 2013). FWI owes its broadband imaging power to the availability of diving waves and low frequencies, which contribute to bridging the sensitivity gap between the smooth and rough components of the subsurface model, the former controlling the wavefield kinematics, the latter producing reflections (Jannane et al., 1989). Seismic reflection data, however, are generated by limited-bandwidth sources, and acquired by limited-length receiver streamers deployed in proximity of the sea-surface. In such context, FWI fails to recover the mid-to-long wavelength model beyond the shallow depths sampled by diving waves (Mora, 1989; Jannane et al., 1989); at greater depths, the FWI sensitivity kernels are dominated by high-wavenumber migration isochrones and, therefore, the inversion behaves similarly to a least squares migration. Reflection FWI (RWI) (Chavent et al., 1994; Xu et al., 2012; Brossier et al., 2015) exploits the wavepaths generated by a prior reconstructed reflective subsurface to build a smooth velocity ( $V_p$ ) field between reflection-generating interfaces and the surface. Joint FWI (JFWI, Zhou et al., 2015) complements the RWI sensitivity kernel at shallow depths by simultaneously exploiting diving and reflected seismic phases.

Both RWI and JFWI achieve smooth  $V_p$  model updates by reformulating the objective function in order to enhance the tomographic component of the gradient over the high-frequency migration kernel (Brossier et al., 2015; Vigh et al., 2019). As demonstrated by Zhou et al. (2015), a velocity-impedance ( $V_p$ - $I_p$ ) parametrization further enables the decoupling between the velocity macromodel and the reflective component of the subsurface. These methodologies are applied within a cycle workflow, whereby the  $I_p$  perturbation model is imaged in the current  $V_p$ , and velocities are then inverted for by JFWI using the updated  $I_p$  reflective model. Alternatively, the inversion can be cast in the pseudo-time domain, thereby exploiting the zero-offset invariance of reflection traveltimes (Plessix, 2013). JFWI is not immune to the inherent non-linearity of waveform inversion with respect to the model long wavelengths (Zhou et al., 2015), and benefits from the use of objective functions robust to cycle-skipping, such as cross-correlation time-shift (e.g., Wang et al., 2019) and optimal transport distance (e.g. Li et al., 2019b).

In this paper, we attempt to reconstruct a complex velocity model comprising a multilayered low-velocity zone and a deep anticline fold, starting from a 1D velocity model, using synthetic limited offset (0.2-5.7 Km) streamer data. The proposed strategy combines JFWI with a graph-space Optimal Transport (GSOT) objective function (Métivier et al., 2019). The GSOT-JFWI solution is then used successfully as starting model for broadband  $V_p$ -FWI, which otherwise fails to converge to the true model. We show that, in the same experiment,  $L^2$ -norm JFWI suffers from severe cycle-skipping, and that JFWI outperforms RWI thanks to the constraints provided by the diving waves in the shallow subsurface.

## METHODOLOGY

### Velocity model building by joint FWI

The JFWI strategy, developed by Zhou et al. (2015), consists in the simultaneous inversion of early arrivals and reflected waves in order to inform the velocity model building with tomographic components sampling both the shallow (diving waves) and deep (reflections) parts of the subsurface. This is combined with a ( $V_p$ - $I_p$ ) parametrization enhancing the scale separation between low and high wavenumbers of the model. The objective function of JFWI is a weighted sum of early arrivals ( $e$ ) and reflections ( $r$ ):

$$C[V_p] = F(W^e(d_f - d_p[V_p, I_{p,0}])) + F(W^r(d_f - d_p[V_p, I_p])), \quad (1)$$

where:  $F$  indicates the chosen objective function;  $W^e$  and  $W^r$  are the weights applied to select early arrivals and reflections respectively;  $d_f$  is the field data and  $d_p$  is the data predicted in the current model, without reflectors if  $I_{p,0}$  is used, with reflectors if  $I_p$  is used instead.

## $V_p$ model building by GSOT-JFWI

By neglecting high-order scattering effects, the sensitivity kernel of Eq.1 with respect to  $V_p$  reads:

$$\nabla C[V_p] = u_0 \star \lambda_0^e + u_0 \star \delta \lambda^r + \delta u \star \lambda_0^r, \quad (2)$$

where: 1) the first term of the right hand side represents the diving wave first Fresnel zone resulting from the cross-correlation of the incident field  $u_0$  and the background adjoint  $\lambda_0^e$  generated by the diving wave residuals; 2) the second term of the right hand side is the source-to-reflector rabbit ear resulting from the cross-correlation of the incident wavefield  $u_0$  and the scattered adjoint wavefield of the reflection residuals  $\delta \lambda^r$ ; 3) the third term of the right hand side is the receiver-to-reflector rabbit ear resulting from the cross-correlation of the scattered primary wavefield  $\delta u$  and the background incident adjoint of the reflection source  $\lambda_0^r$  (Brossier et al., 2015).

The JFWI gradient, unlike Born modeling approach or up-down-going wave separation techniques (Vigh et al., 2019), achieves smooth velocity updates using a full-wavefield adjoint method in two steps (Zhou et al., 2015):

1.  $G_1$ : cross-correlation of the primary  $u_0 + \delta u$  and adjoint field  $\lambda_0^r + \delta \lambda^r$  computed in  $(V_p, I_p)$  and containing both the migration isochrones  $\lambda_0^r \star u_0$  and the RWI kernel (last two terms in Eq.2).
2.  $G_2$ : cross-correlation of the primary  $u_0$  and adjoint field  $\lambda_0^e - \lambda_0^r$  computed in the smooth model  $(V_p, I_{p,0})$ , containing the diving wave Fresnel zone (first term in Eq.2) and the *negative* migration isochrones.

Finally,  $\nabla C(V_p) = G_1 + G_2$  cancels out the migration kernel thanks to the negative sign of  $\lambda_0^r$  in  $G_2$ , yielding the tomographic gradient of Eq.2.

Since JFWI requires  $I_p$  to be known (Eq 2), velocity model building unfolds in cycles: at each round,  $I_p$ -inversion (IpWI) is performed in the current  $V_p$  model as FWI of the short-spread reflections; JFWI then uses the updated  $I_p$  as a-priori reflective model, repeating the cycle until a satisfactory data fitness is obtained.

### A graph-space OT objective function

The Optimal transport distance (OT, Kantorovich, 1942) is convex with respect to shifted patterns in two distribution of positive quantities. However, its adaptation to oscillatory signed signals is not straightforward, and generalizations of OT for seismic inversion are often detrimental to its convexity properties, or of difficult application to field data (Métivier et al., 2018). Graph-space OT (Métivier et al., 2019) circumvents this limitations by transforming the amplitude into a spatial attribute, and treating each seismic trace as discrete 2D cloud of  $K$  points in the time-amplitude  $(t, a)$  plane. For each trace, a linear assignment problem between  $d_f$  and  $d_p$  is solved for the optimal mapping plan  $\sigma^*$ . The 2-Wasserstein based graph-space optimal transport distance  $h_{W2}$  is then defined as a non-local 2D measure of the distance between predicted and observed trace through the assignment  $\sigma^*$ :

$$h_{W2} = \sum_{i=1}^K |t_i - t_{\sigma^*(i)}|^2 + \frac{\Delta t}{A} |a_i^p - a_{\sigma^*(i)}^f|^2 \quad (3)$$

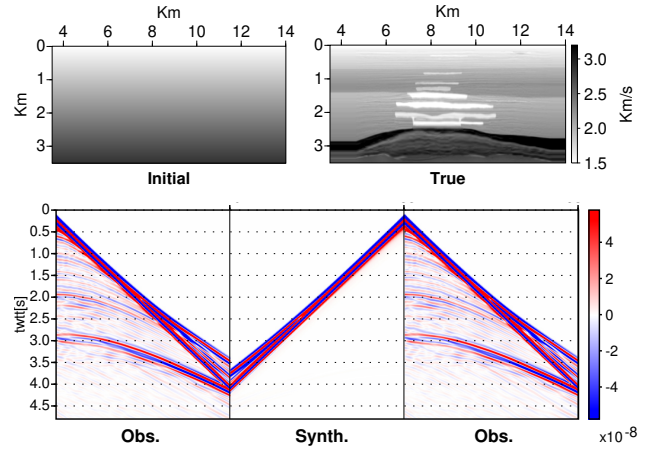


Figure 1: **Data and models.** Top row: start and true  $V_p$ -models. Bottom row: observed shot gather vs synthetic at  $x=8$  Km; obs. is repeated twice and synth. flipped to allow for comparison at long and short offsets.

where the amplitude contribution is scaled by the ratio between the maximum expected time shift  $\Delta t$  and the maximum amplitude  $A$  in both observed and predicted data. Large  $\Delta t$  values emphasize the convexity with respect to shifted patterns and therefore shall help to mitigate cycle skipping, whereas, as  $\Delta t$  decreases,  $h_{W2}$  approximates the behavior of the  $L^2$  distance. Finally, the GSOT misfit function is the summation of  $h_{W2}$  over  $N_s$  sources and  $N_r$  receivers, reweighted to honor trace-by-trace amplitude variations:

$$F_{GSOT}(V_p) = \sum_s^{N_s} \sum_r^{N_r} \zeta_{s,r} h_{W2} \left( a_{s,r}^p, a_{s,r}^f \right) \quad (4)$$

where  $\zeta$  is the weight for each trace.

An important property of GSOT is that its adjoint source is equivalent to the data residuals between samples connected through  $\sigma^*$  (Métivier et al., 2019). In this context, the classic  $L^2$  adjoint source can be considered as a particular case of GSOT in which the data residual is computed sample-by-sample instead of through an optimal transport mapping. Therefore, as observed by Li et al. (2019b), a well parametrized GSOT-FWI is expected to have a similar resolution as a  $L^2$ -FWI despite its robustness against phase ambiguities.

### VALHALL 2D SYNTHETIC

Synthetic surface streamer data have been generated on the synthetic Valhall 2D acoustic model ( $V_p$  and density), simulating a marine streamer acquisition: 128 shots are fired at 110 m spacing and the wavefield is recorded by a 229 channels streamer moving along with the source with group interval equal to 25 m, for an offset range between 80 and 5700 m. The source signature is a zero-phase Ricker with central frequency equal to 6.25 Hz. Full waveform modeling is performed with a 4th order finite-difference scheme ( $dx = 12.5m$ ,  $dt = 2ms$ ), PML absorbing boundaries and no free-surface. The starting model is one-dimensional, and it comprises a water layer ( $V_p=1500 \text{ m.s}^{-1}$ ,  $\text{density}=1 \text{ g/cm}^3$ ) below which  $V_p$  increases linearly with depth; starting density below seafloor is constant and equal to  $2 \text{ g/cm}^3$ , therefore the initial  $I_p$  is simply a scaled

## $V_p$ model building by GSOT-JFWI

version of  $V_p$ . Fig.1 illustrates that the corresponding predicted data are reflection-free and cycle skipped at intermediate-to-large offsets.

### JFWI-IpWI workflow

Data preparation requires the separation of reflected and early wave arrivals, in order to compute the two adjoint sources of the JFWI gradient (Eq.2). The time-limit between the two propagation regimes is defined as the first break arrival time of the direct wave plus the wavelet duration. This is true as long as no post-critical reflections are observed in the data, which is the case in this short offset configuration. Since water-layer velocity is fixed during inversion, such limit is fixed as well. The relative contribution of the two JFWI misfit terms (Eq.1) is balanced by applying a scaling factor of 0.3 to the the diving wave residuals.

The workflow is implemented as cycles of  $I_p$  waveform inversion (IpWI) and JFWI. This strategy benefits from an appropriate data-weighting, whereby the short spread reflections are inverted for  $I_p$ , and the mid-to-long offsets for the smooth  $V_p$  model. This attempts to attenuate the conflict between fixed reflection depth and velocity update in the JFWI stage (Brossier et al., 2015; Zhou et al., 2015). As  $V_p$  approaches the true model, the latter constraint can be relaxed (Li et al., 2019b). The cycle workflow is summarized below:

1. Initialize: source-receiver offset limit [ $lim(i) = 800m$ ]; misfit choice for JFWI [ $Obj$ ] (either GSOT or  $L^2$ )
2. At cycle  $i_{th}$ , data offsets  $< lim(i)$  are inverted for  $(I_p)_{(i)}$  using the current  $(V_p)_{(i-1)}$  model. IpWI is run for 20 iterations of depth preconditioned-LBFGS with an  $L^2$ -norm objective function
3. The updated  $I_p$  is used as a-priori reflective model and data offsets  $> lim(i)$  are inverted for smooth  $V_p$ . JFWI is run for 8 iterations using a depth preconditioned non-linear conjugate gradient with the chosen  $Obj$
4.  $i = i + 1$ . Update  $lim(i)$  in order to include larger portions of the data as the inversion progresses.

If a GSOT objective function is chosen,  $\Delta t$  (Eq.3) is initialized at 0.25 s and progressively reduced down to 0.05 s in order to enhance the robustness to cycle skipping in the initial iterations and progressively converge towards an objective function similar to  $L^2$  (Métivier et al., 2019).

### Results

$L^2$ -JFWI identifies a low velocity zone between 1.5 and 2.5 km depth, as well as a velocity increase corresponding to the bedrock anticline; however, the inversion is not robust to phase ambiguity, as it appears in the cycle-skipped early arrival at long offsets (compare synthetic data in Fig.1 and 2) and the model quality is poor (Fig.2). GSOT-JFWI (Fig.3), provides a high-fidelity macromodel reconstruction, and predicted data show that wavefield kinematics is updated in the correct direction. In Fig.4, the results obtained by GSOT-JFWI and reflection-only GSOT-RWI are compared at three locations extracted from the central part of the model. Note that not only does JFWI improves the shallow model reconstruction, but also it is beneficial to the imaging of the deeper structures, in

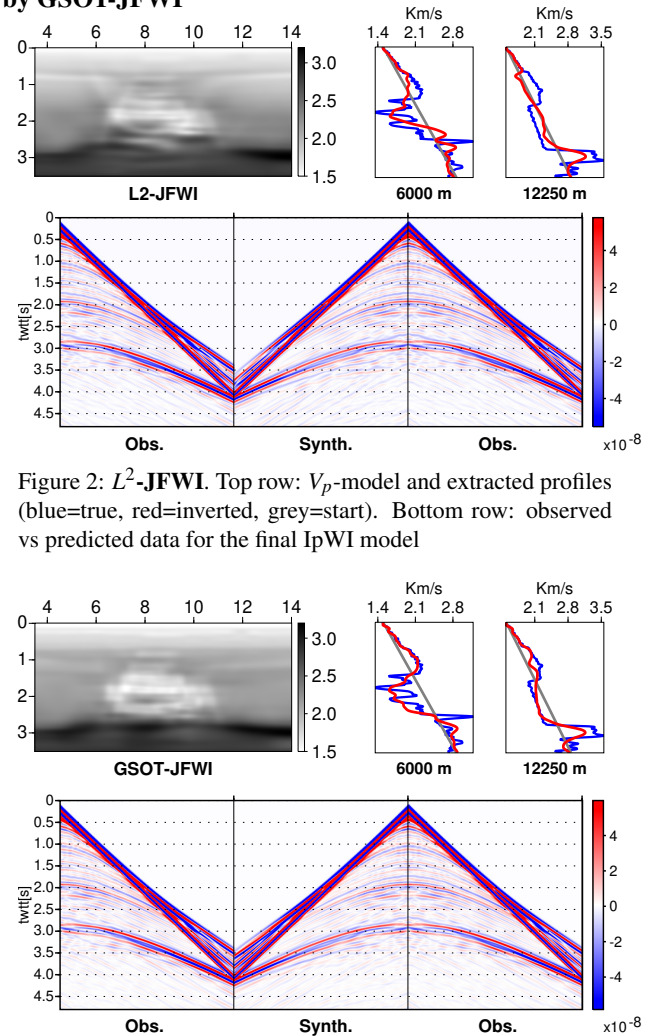


Figure 2:  $L^2$ -JFWI. Top row:  $V_p$ -model and extracted profiles (blue=true, red=inverted, grey=start). Bottom row: observed vs predicted data for the final IpWI model

Figure 3: GSOT-JFWI. Top row:  $V_p$ -model and extracted profiles (blue=true, red=inverted, grey=start). Bottom row: observed vs predicted data for the final IpWI model

particular the geometry of the top of the anticline at 2.5 Km depth.

### $V_p$ -FWI broadband imaging

Here we compare the performance of  $L^2$ -based and GSOT-based JFWI as a means to build an accurate starting model for  $V_p$ -FWI. The role of JFWI is to provide the FWI of limited-offset data with the  $V_p$  low wavenumbers necessary to converge to the broadband solution, and the starting density model is derived using a Gardner's law. The inversion runs for 50 iterations of  $L^2$ -based depth preconditioned  $l$ -BFGS optimization. Fig.5 illustrates the results obtained when using the initial model (Fig.1) as a start of  $V_p$ -FWI. Despite the robustness to cycle-skipping, GSOT-FWI, though outperforming  $L^2$ -based inversion, cannot make up for the lack of low wavenumbers sensitivity and fails to attain a satisfactory solution. In this experiment, FWI provides broadband imaging only if the JFWI macromodels are input as starting models. As expected, the GSOT-JFWI starting model ensures higher quality results than the  $L^2$ -based counterpart (Fig.6). The latter is not accurate

## $V_p$ model building by GSOT-JFWI

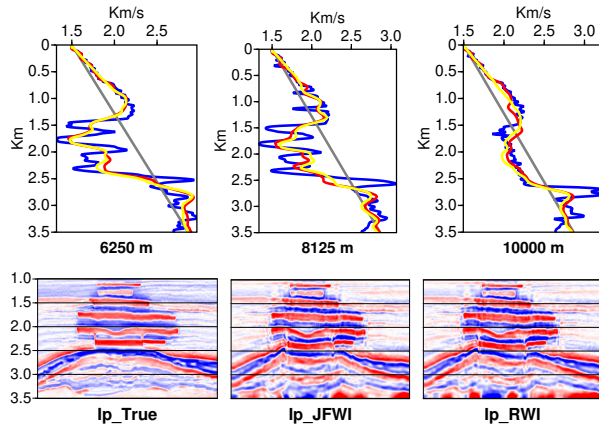


Figure 4: **GSOT-RWI vs GSOT-JFWI**. Top row: extracted velocity profiles (blue=true, grey=start, red=JFWI, yellow=RWI). Bottom row: comparison of final IpWI imaging vs true  $I_p$ .

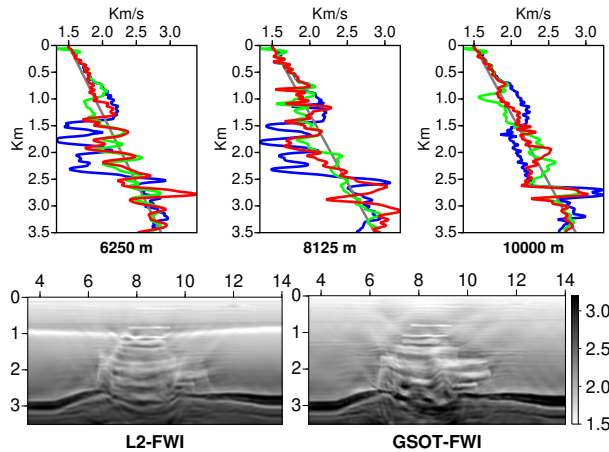


Figure 5:  **$V_p$ -FWI from initial model**. Extracted  $V_p$  profiles (blue=real, grey=start, green= $L^2$ -FWI, red=GSOT-FWI). Bottom row:  $L^2$ -FWI and GSOT-FWI  $V_p$ -models

enough to prevent cycle skipping, whereas GSOT-JFWI+ $L^2$ -FWI attains a quasi-perfect data prediction (Fig.7).

### CONCLUSIONS

This paper presents synthetic tests aiming at the broadband imaging of complex synthetic subsurfaces using limited-offset surface reflection data, starting from a highly non-informative solution. The results show that joint inversion of diving and reflected waves is an effective means to retrieve the tomographic components of the subsurface velocity model. An appropriately parametrized graph-space optimal transport misfit ensures convergence to the true velocity macromodel (Fig.3), whereas  $L^2$ -based inversion is trapped in a local minimum due to cycle-skipping (Fig.2). JFWI outperforms RWI, thanks to the constraints provided by the diving waves in shallow velocity reconstruction. This is beneficial to the imaging of shallow as well as deep targets, as demonstrated by the reconstruction of the anticline geometry in the synthetic model (Fig.4). FWI, starting from the initial one-dimensional model, fails to obtain broadband subsurface imaging regardless the objective func-

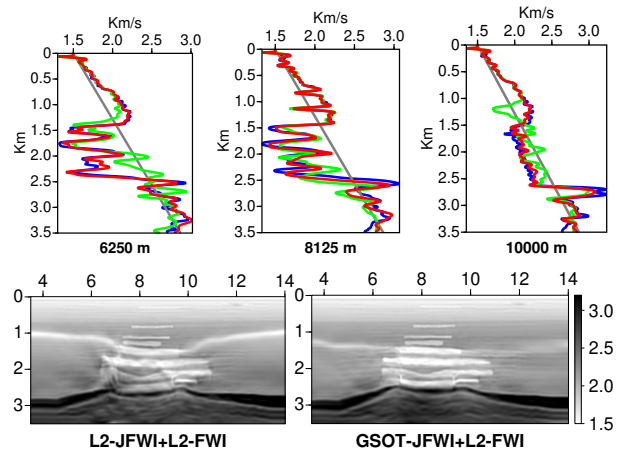


Figure 6:  **$V_p$ -FWI from  $L^2$ - and GSOT-JFWI**. Extracted  $V_p$  profiles (blue=real, grey=start, green= $L^2$ -JFWI+ $L^2$ -FWI, red=GSOT-JFWI+ $L^2$ -FWI). Bottom row:  $L^2$ -FWI  $V_p$ -models starting from  $L^2$ -JFWI and GSOT-JFWI

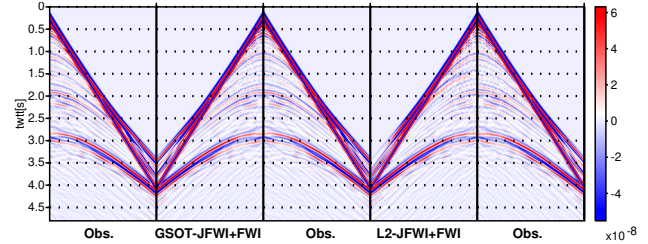


Figure 7: **Data comparison**. Observed data vs Predicted for a shot at  $x=8$  Km, after GSOT-JFWI+ $L^2$ -FWI and  $L^2$ -JFWI+ $L^2$ -FWI

tion used, as a consequence of the lack of transmission-regime seismic phases in the data (Fig.5). JFWI exploits both the diving and the reflected waves to fill the mid-to-long wavelength sensitivity gap of surface reflection seismic data and allows FWI to converge to a broadband solution (Fig.6).

Future work will aim at the application to real streamer 2- and 3-D datasets, along with improvements in computational efficiency: 1) approximate inverse  $I_p$ -preconditioner (Li et al., 2019a) to speed up convergence in the IpWI stage; 2) structure-oriented  $V_p$ -JFWI gradient smoothing (Trinh et al., 2017), exploiting the subsurface geometries imaged by IpWI at each cycle; 3) pseudo-time domain implementations, avoiding the inconsistency between fixed reflectivity and velocity update at each JFWI cycle (Brossier et al., 2015).

### ACKNOWLEDGMENTS

This study was partially funded by the SEISCOPE consortium (<https://seiscope2.osug.fr>), sponsored by AKERBP, CGG, CHEVRON, EQUINOR, EXXON-MOBIL, JGI, PETROBRAS, SCHLUMBERGER, SHELL, SINOPEC, SISPROBE and TOTAL. This study was granted access to the HPC resources of CIMENT infrastructure (<https://ciment.ujf-grenoble.fr>) and CINES/IDRIS/TGCC under the allocation 046091 made by GENCI.

## REFERENCES

- Brossier, R., S. Operto, and J. Virieux, 2015, Velocity model building from seismic reflection data by full waveform inversion: *Geophysical Prospecting*, **63**, 354–367, doi: <https://doi.org/10.1111/1365-2478.12190>.
- Chavent, G., F. Clément, and S. Gómez, 1994, Automatic determination of velocities via migration-based traveltime waveform inversion: A synthetic data example: 64th Annual International Meeting, SEG, Expanded Abstracts, 1179–1182, doi: <https://doi.org/10.1190/1.1822731>.
- Jannane, M., W. Beydoun, E. Crase, D. Cao, Z. Koren, E. Landa, M. Mendes, A. Pica, M. Noble, G. Roeth, S. Singh, R. Snieder, A. Tarantola, and D. Trezeguet, 1989, Wavelengths of Earth structures that can be resolved from seismic reflection data: *Geophysics*, **54**, 906–910, doi: <https://doi.org/10.1190/1.1442719>.
- Kantorovich, L., 1942, On the transfer of masses: *Dokl. Acad. Nauk. USSR*, **37**, 7–8.
- Lailly, P., 1983, The seismic problem as a sequence of before-stack migrations: Presented at the Conference on Inverse Scattering: Theory and Applications, SIAM.
- Li, Y., R. Brossier, and L. Métivier, 2019a, Combining approximate inverse and joint full waveform inversion for velocity model building: 81th Annual International Conference and Exhibition, EAGE, Expanded Abstracts, Th P01 05, doi: <https://doi.org/10.3997/2214-4609.201901342>.
- Li, Y., R. Brossier, and L. Métivier, 2019b, Joint FWI for imaging deep structures: A graph-space OT approach: 89th Annual International Meeting, SEG, Expanded Abstracts, 1290–1294, doi: <https://doi.org/10.1190/segam2019-3206304.1>.
- Métivier, L., A. Allain, R. Brossier, Q. Mérigot, E. Oudet, and J. Virieux, 2018, Optimal transport for mitigating cycle skipping in full waveform inversion: a graph space transform approach: *Geophysics*, **83**, R515–R540, doi: <https://doi.org/10.1190/geo2017-0807.1>.
- Métivier, L., R. Brossier, Q. Mérigot, and E. Oudet, 2019, A graph space optimal transport distance as a generalization of L<sub>p</sub> distances: application to a seismic imaging inverse problem: *Inverse Problems*, **35**, 085001, doi: <https://doi.org/10.1088/1361-6420/ab206f>.
- Mora, P. R., 1989, Inversion = migration + tomography: *Geophysics*, **54**, 1575–1586, doi: <https://doi.org/10.1190/1.1442625>.
- Operto, S., R. Brossier, Y. Gholami, L. Métivier, V. Prieux, A. Ribodetti, and J. Virieux, 2013, A guided tour of multiparameter full waveform inversion for multicomponent data: from theory to practice: The Leading Edge, Special section Full Waveform Inversion, 1040–1054, doi: <https://doi.org/10.1190/tle32091040.1>.
- Plessix, R. E., 2013, A pseudo-time formulation for acoustic full waveform inversion: *Geophysical Journal International*, **192**, 613–630, doi: <https://doi.org/10.1093/gji/ggs056>.
- Tarantola, A., 1984, Inversion of seismic reflection data in the acoustic approximation: *Geophysics*, **49**, 1259–1266, doi: <https://doi.org/10.1190/1.1441754>.
- Trinh, P. T., R. Brossier, L. Métivier, J. Virieux, and P. Wellington, 2017, Bessel smoothing filter for spectral element mesh: *Geophysical Journal International*, **209**, 1489–1512, doi: <https://doi.org/10.1093/gji/ggx103>.
- Vigh, D., X. Cheng, K. Jiao, and D. Sun, 2019, Keys to robust reflection-based full-waveform inversion: 81st Annual International Conference and Exhibition, EAGE, Expanded Abstracts, doi: <https://doi.org/10.3997/2214-4609.201900877>.
- Virieux, J. and S. Operto, 2009, An overview of full waveform inversion in exploration geophysics: *Geophysics*, **74**, WCC1–WCC26, doi: <https://doi.org/10.1190/1.3238367>.
- Wang, C., P. Farmer, D. Yingst, I. Jones, C. Calderon, and J. Brittan, 2019, Preconditioned reflection full waveform inversion for subsalt imaging: 81st Annual International Conference and Exhibition, EAGE, Expanded Abstracts, doi: <https://doi.org/10.3997/2214-4609.201900868>.
- Xu, S., D. Wang, F. Chen, G. Lambaré, and Y. Zhang, 2012, Inversion on reflected seismic wave: 82nd Annual International Meeting, SEG, 1–7, doi: <https://doi.org/10.1190/segam2012-1473.1>.
- Zhou, W., R. Brossier, S. Operto, and J. Virieux, 2015, Full waveform inversion of diving & reflected waves for velocity model building with impedance inversion based on scale separation: *Geophysical Journal International*, **202**, 1535–1554, doi: <https://doi.org/10.1093/gji/ggv228>.